Hematite porous architectures as enhanced air purification photocatalyst

José Balbuena,[a] Manuel Cruz-Yusta,[a] Ana L. Cuevas,[b] Francisco Martín,[c], Adrián Pastor,[a] Rocío Romero [b] and Luis Sánchez [a],**

a) Departamento de Química Inorgánica, Instituto Universitario de Investigación en Química Fina y Nanoquímica IUIQFN, Universidad de Córdoba, Campus de Rabanales, E-14071 Córdoba, España.
b) Unidad de Nanotecnología. Edificio de Bioinnovación. Universidad de Málaga - Málaga, 29071, Spain.
c) Chemical Engineering Department, Campus de Teatinos, Universidad de Málaga- Málaga, 29071, Spain.

* Corresponding Author:

- Prof. Luis Sánchez

  ORCID ID: 0000-0002-0194-1908

  Departamento de Química Inorgánica, Instituto Universitario de Investigación en Química Fina y Nanoquímica IUIQFN, Universidad de Córdoba, Campus de Rabanales, E-14071 Córdoba, España.

  E-mail: luis-sanchez@uco.es

  Tel: +00-34-957-218634

ABSTRACT

Different α-Fe_2O_3 porous architectures were obtained by electrospinning (nanotubes) or without electrospinning (flakes), and heating treatments using $Fe(NO_3)_2$/PVP (Polyvinylpyrrolidone) as a precursor. The particles constituting the nanotubes and flakes samples exhibited similar wall porosity and crystal size, while the existence of the micropore area was also a characteristic. The chemical identity was confirmed as hematite by XRD, Raman and XPS studies. The prepared samples were studied as photocatalytic materials in the removal of NO_X gases from air, their De-NO_X ability being superior to that previously reported for hematite photocatalysts. These porous hematite samples exhibited a high NO conversion efficiency and similar to that of TiO_2 P25, this being the first report for α-Fe_2O_3 oxide. Additionally, the calculated De-NO_X selectivity values were higher than that of TiO_2 P25. The adsorption of NO_2 molecules is facilitated on these porous architectures, assisting in the enhancement of the of the photochemical process selectivity.

Keywords

Iron oxide, Photocatalytic oxidation, Nitrogen oxides

1. Introduction

Air quality, or in other words its degradation or pollution, is the result of complex phenomena derived from a plurality of causes and effects generally associated with human activity and the emission of pollutants into the atmosphere. Currently, cities fight against serious pollution problems in their urban atmosphere, due to emissions from transport systems and industry. In fact, transport systems are becoming the main source of nitrogen oxides (NO_X = NO + NO_2) pollutant emissions [1]. Unfortunately, despite the adversative and dangerous effects associated with its presence in the atmosphere [2, 3], the recommended maximum amount of breathable NO_X is still often exceeded, especially in large cities [4, 5], rendering the efficient removal of NO_X one of the main open challenges.

Over the past years, the photocatalytic oxidation (PCO) of NO_X emissions has been recognized as being a potent and simple technology to remove NO_X gases from the atmosphere, known as De-NO_X action [6-8]. Thus, the photochemical NO_X oxidation is easily promoted by using only a TiO_2 photocatalyst, atmospheric oxygen, water, and UV-A radiation [9, 10]. On this basis, building materials such as photocatalytic pavements, cement, mortars, and paints are designed as tools to combat NO_X pollution in our cities [11, 12]. The future implementation of De-NO_X materials in our cities, a large-scale operation, would prevail when low-cost materials with the highest photocatalytic efficiency (under UV and Vis light irradiation) were developed [13-15]. In this sense, an interesting alternative to TiO_2 is iron oxide.

The iron oxide (III) hematite phase (α-Fe_2O_3; $E_G \approx 2.1$ eV) has emerged as an appealing candidate, thanks to its easy accessibility, abundance, low cost and biocompatibility [16]. It is known that properties of the α-Fe_2O_3 – surface structure, including surface area, porosity and morphology; crystal size and defects; doping or the presence of impurities – together with the experimental parameters of synthesis have an influence on their photocatalytic activity [16]. It is also known that outstanding photocatalytic performances were found through the

preparation of nanoarchitectures [17-22]. Recently, our research group reported the 1D nanoarchitecture of hematite as a De-NO_X photocatalyst [23], empowering the NO_X removal efficiency reported in the past [24]. Now, we focus our attention on the improvement of De-NO_X response by changing its microstructure. As it was previously reported for TiO_2, designing an appropriate porous microstructure resulted in enhanced photocatalytic activity in both aqueous and gas media reactions [10, 25, 26]. The present work is devoted to the preparation of singular hematite porous architectures with different dimensionality – nanotubes and flakes – exhibiting an outstanding efficiency as a De-NO_X photocatalyst. The chemical, physical and optical properties of the samples were characterized. For the first time, thanks to this singular porous architecture, hematite shows similar NO removal efficiency to that exhibited by the TiO_2 P25 standard photocatalyst. Moreover, porous hematite exhibited higher De-NO_X selectivity than titania.

2. Experimental

2.1 Preparation of hematite samples

The hematite electrospun nanotubes (H_nanotubes) were obtained by electrospinning using a BERTAN power source 225-30R model. The precursor solution was composed of 2 g Iron (II) nitrate nona-hydrate in PVP (Polyvinylpyrrolidone), dissolved in 40 mL of ethanol and 10 mL H_2O. PVP solution was prepared using 5 g of 1.300.000 Mw PVP. The electrical potential, with negative polarity in the active electrode, was 30 kV. A fast thermal treatment was performed by introducing the as-obtained electrospun PVP fibres in a preheated oven at 350 °C in order to avoid melting creep and sticking, followed by a heating slope of 15 °C·min^{-1} to 650 °C and kept at this temperature for 3 h. Hematite flakes (H_flakes) were prepared using the same polymer solution as sample H_ nanotubes without using the electrospun technique. Thus, the precursor solution was calcined following a multi-step heating sequence: at 100 °C, 200 °C and

300 °C, maintaining a constant temperature for 30 min for each step and, finally, increasing the temperature (with a 15 °C·min^{-1} slope) to 650 °C and then keeping it at this temperature for 3 h. For comparison purposes, a commercial photocatalytic additive, Aeroxide® TiO_2 P25 (Evonik), was also used.

2.2 Instrumentation

The identification of crystalline phases and the average crystallite size were achieved using X-ray diffraction (XRD) on a Siemens D5000 X-ray diffractometer with CuKα1,2 radiation. The crystal structure and the average crystallite size of the samples were estimated using the Rietveld and Williamson-Hall methods. Scanning electron microscopy (SEM) images were obtained with a FEI Helios Nanolab 650 FESEM microscope and high-resolution transmission electron microscopy (HRTEM) images were recorded using a JEOL-2010. Nitrogen absorption isotherms were obtained at 77.4 K on an ASAP 2020 instrument from Micromeritics. Infrared spectra, IR, transmittance mode with normal incidence, were obtained using a Perkin Elmer FTIR System Spectrum BX. Raman spectra were recorded by a Raman spectrometer (SENTERRA) with a confocal microscope (Olympus BX series) using 785 nm to avoid fluorescence. X-ray photoelectron spectra were recorded using a Physical Electronics PHI 5700 spectrometer.

2.3 Photocatalysis

The photocatalytic activity of the materials towards the oxidation of NO was studied by using a 50 x 50 mm sample holder placed in a laminar flow reactor. The reactor was placed inside a light sealed irradiation box (Solarbox 3000e RH) equipped with a Xe lamp **(300 – 825 nm spectral emission)** with controlled irradiance. A 10 mg sample was used in each photocatalytic test. Artificial sunlight (25 and 550 W·m^{-2} for UV and visible irradiances, respectively) was used

as the irradiation source. **Air was conveyed by a gas-washing bottle, filled with demineralised water in order to keep the relative humidity of the supplied gas fixed at 50 ± 5%.** A mixture of air/NO was sent to the photoreactor. Synthetic air and NO gas streams were mixed to obtain the desired NO concentration **(150 ppb). The accurate measurement of the concentration of NO, NO_X and NO_2 was carried out using a chemiluminescence analyser (model Environnement AC32M); a flow rate, *Q*, of 0.30 L min^{-1} was employed.** The photocatalytic efficiency was evaluated following the NO conversion (%), NO_2 released (%) and NO_X conversion (%) parameters (defined in Electronic Supplementary Information; ESI).

Additional information about methods is provided in ESI.

3. Results and discussion

3.1 Samples characterisation

As previously reported, the final diameter of the solid α-Fe_2O_3 electrospun fibres is dependent on the initial PVP fiber diameter and the concentration of the iron oxide precursor, decreasing with the concentration of the iron compound in the polymer [27-29]. However, using higher molecular weight PVP (Mw = 1,300,000) increases the solution viscosity, for the same initial concentrations of PVP and Fe precursor (water solution) in the ethanol solvent, which leads to mats of thicker PVP fibres being obtained than by using lower PVP Mw. Depending on the rate of the heating treatment, the initial electrospun PVP fibre mat is converted into a mat of **Fe_2O_3 interconnected nanotubes**, Figs. 1a and 1b **(H_nanotubes sample)**. The influence of the heating rate in the formation and morphology of the hollow fibres was previously reported [30]. At a lower heating rate, the fibre is homogenously heated, leading to shrinkage of its diameter. At higher heating rates, the electrospun fibres form an outer crust preventing further contraction of the outer diameter, while the inner polymer continues shrinking, undergoing two simultaneous forces: cohesive and adhesive. When the adhesive is stronger

than the cohesive force, then the shrinking would be outward the preformed crust, resulting in a hollow fibre. The prevalence of cohesive forces, or no formation of the outer preformed crust, results in reduced diameter and solid fibres. This high rate of heating was carried out by introducing the electrospun fibres in a preheated oven at 350 °C, followed by a heating rate of 15 °C·min^{-1} to 650 °C, and maintained at 650 °C for 3 hours. On average, **for this H_nanotubes sample,** the outer diameter of the nanotubes was in the 200 – 500 nm range (mean 317 nm, standard deviation 110 nm). **However**, a few **tubes** reach the highest dimensions shown in Fig. 1c, with an outer diameter of 2.3 µm and wall thickness of 120 nm**, corresponding to microtubes (Figs 1c and, 1d)**. This sometimes happens because lateral fusion of several nanotubes. The wall of the nanotubes exhibited a smooth external surface and a porous interior, Figs. 1c and 1d and Fig. S1.

On the other hand, powders resembling flakes were obtained when electrospinning was not used and the polymer precursor solution was directly calcined as previously described. The flakes showed a stacked structure of lamellas, as shown by low magnification optical microscopy (Fig. S2). In the higher magnification of the electron microscopy (Fig. 2), some rolled lamellas of hematite (Fig. 2a and 2b) and mainly, porous flat lamellas (Figs. 2c and 2d) with a thickness of around 1 µm (Fig. 2d) were observed. The laminar structure, that forms the flakes, could be produced by self-assembly of the PVP with the polar solvent ethanol/water (iron nitrate), as it is known that the polarity of the solvent has an effect on the assembly behaviour of the PVP. In fact, PVP is an amphiphilic molecule with the amide groups in the pyrrolidone rings as hydrophilic groups and the hydrocarbon chains as hydrophobic groups [31-33].

In both cases, the wall of the nanotubes and the lamellas (which forms the flakes) were highly porous. It has been proposed that ternary systems containing a highly volatile solvent and a less volatile solvent mixed with the polymer create porosity [34] because of the difference in evaporation rates and by thermally-induced phase separation. If the sample is quickly heated,

a crust is formed. The layer which forms the "skin" of the crust acts as a barrier against the diffusion of components , causing slower coagulation in the bulk resulting in a highly porous structure below the skin [35], as observed for H_nanotubes and H_flakes samples. A similar particle pattern of the wall cross-section of the nanotubes and lamellas (Figures 1 and 2) could be explained based on spinodal phase separation [36, 37], with spinodal phase separation being characterised by the occurrence of diffusion against a concentration gradient, and porous nanostructures being obtained (Scheme 1) [38],[39]. The Mw of PVP, PVP/precursor concentration ratio, and the polar and water solvent, and the rate of heating would affect the type of thermally induced phase separation and the final morphology [34].

The chemical identity was elucidated as hematite by XRD, XPS and Raman. Fig. 3a shows the XRD pattern corresponding to the prepared samples. All detected peaks were ascribable to the *hkl* reflections of rhombohedral α-Fe_2O_3. The calculated crystal sizes were 54 and 66 nm for H_nanotubes and H_flakes samples, respectively. Comparing these values with those measured from SEM images (Fig. S1) it was concluded that nanotube walls and sheets are constituted by the assembling of independent hematite nanocrystals. Hematite can also be easily distinguished from other iron oxides or hydroxides using Raman. From the Raman spectra of both samples (Fig. 3b), the bands at 226 and 496 cm^{-1}, (A_{1g} mode) and those at 245, 293, 411, 612 cm^{-1} (E_g mode) correspond to that expected for hematite [40, 41]. No other peaks are detected, discarding the presence of other iron oxides and iron oxyhydroxides.

The chemical composition was confirmed through the study of the corresponding XPS spectra. The XPS spectra of the Fe_{2p} region and Fe_{3p} were identical for both samples. Fig. 3c, as an example, shows those corresponding to the sample H_nanotubes. The broad peaks at 725.4 and 711.3 eV correspond to those reported for $2p_{1/2}$ and $2p_{3/2}$ signals, respectively, of Fe^{3+} in Fe_2O_3 [42]. The satellite signal appeared at 719.2 eV is also expected for Fe_2O_3, whereas a signal at around 715 eV would be consistent with the existence of Fe^{2+} [43]. Moreover, the presence of Fe^{3+} was also corroborated from the spectra of Fe 3p XPS region (Fig. 3c inset).

Only one main peak is registered at 55.6 eV, because the XPS spectrometer does not have the resolution to resolve the $3p_{1/2}$ and $3p_{3/2}$ signals. The deconvolution of the 3p region was carried out considering the Fe $3p_{3/2}$ peak at 55.6 eV. No signal was observed at the binding-energy value expected for Fe^{2+}, that is, at 53.7 eV.

Following the physical characterisation, the porosity of the α-Fe_2O_3 samples was studied from adsorption-desorption isotherms of N_2 at 77K, Fig. 4a. Type II isotherms were obtained for α-Fe_2O_3 samples [44], from which the area of the samples were estimated, Table 1. The observed isotherms are characteristics of low porosity solids, exhibiting a heterogeneous microstructure consisting of micro-, meso- and macropores (Fig 4a inset). It is worth noting that most of the surface area consists of micropores (Table 1 and Fig. 4a). The adsorption-desorption branches show a hysteresis loop, which fits the H3 type characteristic of mesoporous materials, in agreement with the increased pore size distribution observed in the 2.0 – 5.0 nm range. In comparison with the previously reported hematite nano-powders [23, 24], the largest micropore area measured for these samples would be consistent with the promotion of microporosity in the crust of the nanotube/film, because of the spinodal phase separation, as stated above.

Finally, the optical properties of the samples were analysed by reflectance spectroscopy. The acquired diffuse reflectance spectra was converted to the Kubelka-Munk function, $[F(R_\infty)\ hv]^2$. The band gap energy – E_g – of the samples is found plotting $[F(R_\infty)\ hv]^2$ against hv, as is shown in Fig. 4b. For both samples the E_g value was calculated as 2.15 eV, which is very close to the expected 2.2 eV for bulk α-Fe_2O_3 [24].

3.2 NO_X Photocatalytic oxidation test

The NO photo-oxidation efficiency of the α-Fe_2O_3 samples was studied. Recently, our research group validated the ability of hematite towards the photochemical oxidation (PCO) of NO_X

gases [24]. Basically, the photocatalytic oxidation of nitric oxide proceeds from individual one-electron transfer steps, via the intermediate species nitrous acid (HNO_2) and nitrogen dioxide (NO_2). As the α-Fe_2O_3 particles are irradiated by sunlight irradiation, an electron in the valence band (VB) acquires the energy of a photon to become a photogenerated electron (e^-), which migrates to the conduction band (CB) and simultaneously leaves a photogenerated hole (h^+) behind. The pair of mobile charges produced can reach the surface of the semiconductor particle and, in contact with oxygen and water molecules, assisting the formation of reactive oxygen species (ROS). The ROS species (mainly, hydroxyl radicals, but also superoxide) act as strong oxidants in the photochemical mechanism: [8, 24]

$$NO \xrightarrow{OH\bullet} HNO_2 \xrightarrow{OH\bullet} NO_2 \xrightarrow{OH\bullet} NO_3^- \qquad (1)$$

Fig. 5a shows the nitric oxide (NO) concentration profile obtained during the NO oxidation test under light irradiation performed for hematite porous samples. The concentration of NO only experiments a sudden decrease under irradiation meaning that, once the activation of the α-Fe_2O_3 sites occurs, the oxidation of the pollutant took place by the heterogeneous photocatalytic reaction. Fig. S3 shows the NO, NO_2 and NO_X concentration profiles registered during the same test. It is observed that the removal of NO is accompanied by the release of NO_2 gas, an intermediate of the photochemical process but more toxic than NO molecule [45]. Considering both phenomena, the NO_X plot describes the whole amount of nitrogen oxides gases removed. On the other hand, the photochemical mechanism is stated by the identification of NO_2^-/NO_3^- species in the IR spectra of the H_nanotubes sample after irradiation, Fig. S4. New bands in the 1000–1600 cm^{-1} range, concerning N–O vibration modes, appear in the spectra obtained after irradiation. The band located at 1543 cm^{-1} corresponds to vibrations of nitrate specie, the presence of nitrite anions being assigned to 1415 and 1335 cm^{-1} bands. The lowest bands at 1150 and 1041 cm^{-1} must be tentatively assigned to bridging ions [46-48]. The O–H vibrating mode of traces of adsorbed water accounts at 1640 cm^{-1}.

For comparison purposes, the NO removal efficiency of hematite samples was compared to commercial TiO_2 P25 (benchmark photocatalytic material worldwide used as standard on the research field; Fig. 5a, Fig. S3 and Table 1). As was previously known [24], the photocatalytic behaviour of the hematite nano-powders for NO removal is very scarce, around 13 % of efficiency. Through the preparation of nanofibers [23] the NO removal is doubled, however this efficiency seems far from what was expected due to the reported surface area (22.1 $m^2 g^{-1}$). Surprisingly, it was observed that the NO removal efficiency of these hematite porous architectures was so high – five times that reported for hematite nano-powders [24] – and similar to that exhibited by TiO_2 P25. These systems exhibit an NO conversion efficiency ≈70%, which is similar to that exhibited by advanced TiO_2-based systems [49-54]. **As can be noticed from Figure S5 in the Supplementary Information, under Vis Light the NO conversion is limited to 11-14 % and does not occur for TiO_2 P25.**

In spite of their low BET surface area, around 13.7 m^2g^{-1}, the outstanding NO efficiency values found could be explained by considering the porous architecture of both samples, as described for other De-NO_X photocatalysts. This peculiar heterogenous microstructure would facilitate the photo-oxidation of gas molecules in the pores and channels by the just produced hydroxyl radicals. In this sense, the De-NO_X selectivity value, *S* (defined in ESI), a parameter which expresses the ratio of degraded NO that becomes as innocuous nitrate rather than toxic nitrogen dioxide must be interpreted [55]. The *S* values obtained for H_nanotubes and H_flakes were 54 and 51 %, respectively (Fig. 5b). In comparison, the De-NO_X selectivity corresponding to commercial TiO_2 P25 proved to be poor enough after 30 minutes of light irradiation, for which an *S* value of 29 % was found. This is easily understood by observing the nitrogen oxides concentration profiles obtained during the photochemical degradation of NO gas, Fig. S3. In the case of the titania sample, the major part of inlet NO gas is released as NO_2 at the end of the irradiation period, which could also be associated with the very low

proportion of micropore area (Table 1). However, for H-nanotubes and H_flakes samples the micropore area accounts for more than half of the specific surface area (Table 1). The higher S value was reached for H-nanotubes, the sample with the highest micropore area contribution (87%). Moreover, a significant population of mesopores was found for hematite samples, being scarce for TiO_2 P25 (Fig. **S6**). Therefore, it seems reasonable to consider that microporous structure of hematite enhances the photochemical process. It would be assumed that most of the NO molecules are converted into NO_3^-, and not released to the atmosphere as NO_2. The rising number of NO_2 molecules would probably have enough time to be oxidised into NO_3^- because they remain adsorbed on the pores and channels on the hematite surface.

In this sense, additional evidence was obtained from preliminary NO_2 gas adsorption studies. Thus, a mixture of air/NO_2 was sent to the reactor with a NO_2 concentration around 150 ppb, obtained by mixing synthetic air and pure NO_2 (flow rate of 0.30 L min^{-1}; R.H. at 50 ± 5). In the absence of light irradiation, NO_2 gas was passed over the samples and differences were observed in the evolution of the concentration profile with time, Fig. 5c. The NO_2 concentration profile for TiO_2-P25 is similar to that of a blank test (without the presence of catalyst). In both cases, the NO_2 concentration remained constant at the initial inlet value during the time of the experiment, and therefore, there was no interaction between the gas and the catalyst or chamber surface. However, in the case of the H_nanotubes sample (as way of example), lower concentration values for NO_2 were measured during the first 40 minutes indicating that gas molecules are probably being adsorbed on their surface. As aforementioned, the higher De-NO_X selectivity found for porous hematite samples would be explained based on their ability to adsorb the recently formed NO_2 gas molecule (reaction 1), facilitating its oxidation to nitrate before it is released to the atmosphere. A similar relationship between pore microstructure and high De-NO_X efficiency was also previously

stated for TiO_2. Thus, in the case of mesocrystalline anatase nanoparticles, high NO conversion values but also a more selective De-NO_X process were reported [10].

Fig. 5b helps to elucidate the true De-NOx behaviour of the different photocatalysts object to study. This figure plots the amount (%) of NO and NO_X removal, NO_2 released and selectivity values for each sample. The highest amount of NO removal (blue columns) is found for TiO_2 P25, with this being due to the higher photo activity according to its high BET area (Table 1) and, mainly, to the inherent photochemical properties better than those of hematite. In this sense, the characteristic short excited-state lifetime (ca. 1 ps) and small hole-diffusion length (ca. 2–4 nm) of hematite are known to promote fast hole/electron recombination [17], thus limiting in some manner the existence of ROS species to promote reaction (1). However, considering a true environmental remediation, it is of importance to know about the total amount of NO_X gases removed (Fig. 5b; pink columns). Under the measured experimental conditions, because they exhibit the highest *S* values, above 50 %, the H-nanotubes and H_flakes samples are considered to be better photocatalysts, with the photocatalytic behaviour of TiO_2 being hindered by the scarce ability to retain and convert the NO_2 gas (70 % of gas molecules released). Thus, porous hematite samples perform better in the the NO → NO_2 → NO_3^- oxidation process, allowing a higher amount of the whole NO_X gases to be removed, around 40 %, in comparison with TiO_2 P25 (25 % NO_X removed). Moreover, the photocatalyst´s reusability was studied. Several consecutive NO photocatalytic removal experiments were run over H_nanotubes in periods of 30 min, Fig. **S7**. Between experiments, the sample was rinsed with water between consecutive cycles in order to eliminate nitrite/nitrate species. The low activity loss, lower than 8%, is indicative of good reusability. **In the other hand, low photocatalyst inactivation during an extended period of six hours of light irradiation was observed, Fig. S8.**

4. Conclusions

Two different Fe_2O_3 porous architectures, interconnected nanotubes and flakes, have been obtained. Nanotubes were prepared by electrospinning of the $Fe(NO_3)_2$/PVP solution and its subsequent calcination, the α-Fe_2O_3 flakes being obtained by direct calcination of the $Fe(NO_3)_2$/PVP mix. Sintered nanoparticles formed the nanotubes and flakes samples exhibiting similar wall porosity and crystal size and large micropore area. The NO removal accounts through the NO → NO_2 → NO_3^- photo-oxidation process, with significative performance (around 40 %) and reusability. These samples exhibit a high NO conversion efficiency similar to that of TiO_2 P25 and previous reports of other advanced TiO_2 based systems, with this being the first reported for α-Fe_2O_3 oxide. Additionally, the Fe_2O_3 porous architectures showed higher De-NO_X selectivity than TiO_2 P25. In this sense, the good selectivity observed could be related to their large micropore area, facilitating the adsorption of NO_2 molecules.

Appendix A. Supplementary Information

Supplementary Information accompanying this paper includes more information about: morphological characterization of the samples; De-NO_X test for photocatalysts; IR Spectra; Microstructural characterization of TiO_2 P25; De-NO_X cycling test.

Acknowledgements

This work was funded by Junta de Andalucía (FQM174 and RNM-192 research groups) and Ministerio de Economía y Competitividad (TEC2014-53906-R).

References

[1] B. Yang, K.M. Zhang, W.D. Xu, S. Zhang, S. Batterman, R.W. Baldauf, P. Deshmukh, R. Snow, Y. Wu, Q. Zhang, Z. Li, X. Wu, On-Road Chemical Transformation as an Important Mechanism of NO_2 Formation, Environ. Sci. Technol., 52 (2018) 4574-4582.

[2] M.C. Newman, W.H. Clement, Ecotoxicology, in: B. Raton (Ed.) Ecotoxicology, CRC Press, Florida, 2008.

[3] B. Chen, C. Hong, H. Kan, Exposures and health outcomes from outdoor air pollutants in China, Toxicology, 198 (2004) 291-300.

[4] M.W. Frampton, I.A. Greaves, NO_X - NO_X: Who's There?, Am. J. Respir. Crit. Care. Med., 179 (2009) 1077-1078.

[5] M.L. Williams, D.C. Carslaw, New Directions: Science and policy – Out of step on NO_X and NO_2?, Atmos. Environ., 45 (2011) 3911-3912.

[6] S. Devahasdin, C. Fan Jr, K. Li, D.H. Chen, TiO_2 photocatalytic oxidation of nitric oxide: transient behavior and reaction kinetics, J. Photochem. Photobiol. A, 156 (2003) 161-170.

[7] C.H. Ao, S.C. Lee, Enhancement effect of TiO_2 immobilized on activated carbon filter for the photodegradation of pollutants at typical indoor air level, Appl. Catal. B: Environ., 44 (2003) 191-205.

[8] J. Balbuena, M. Cruz-Yusta, L. Sánchez, Nanomaterials to Combat NO_X Pollution, J. Nanosci. Nanotechnol., 15 (2015) 6373-6385.

[9] A. Folli, S.B. Campbell, J.A. Anderson, D.E. Macphee, Role of TiO_2 surface hydration on NO oxidation photo-activity, J. Photochem. Photobiol. A, 220 (2011) 85-93.

[10] J. Balbuena, J.M. Calatayud, M. Cruz-Yusta, P. Pardo, F. Martin, J. Alarcon, L. Sanchez, Mesocrystalline anatase nanoparticles synthesized using a simple hydrothermal approach with enhanced light harvesting for gas-phase reaction, Dalton Trans., (2018).

[11] L. Pinho, M.J. Mosquera, Photocatalytic activity of TiO_2–SiO_2 nanocomposites applied to buildings: Influence of particle size and loading, Appl. Catal. B: Environ., 134–135 (2013) 205-221.

[12] M.M. Ballari, M. Hunger, G. Hüsken, H.J.H. Brouwers, NO_X photocatalytic degradation employing concrete pavement containing titanium dioxide, Appl. Catal. B: Environ., 95 (2010) 245-254.

[13] R. Sugrañez, J.I. Álvarez, M. Cruz-Yusta, I. Mármol, J. Morales, J. Vila, L. Sánchez, Enhanced photocatalytic degradation of NO_X gases by regulating the microstructure of mortar cement modified with titanium dioxide, Build. Environ., 69 (2013) 55-63.

[14] R. Sugrañez, M. Cruz-Yusta, I. Mármol, J. Morales, L. Sánchez, Preparation of Sustainable Photocatalytic Materials through the Valorization of Industrial Wastes, ChemSusChem, 6 (2013) 2340-2347.

[15] C.L. Bianchi, C. Pirola, F. Galli, G. Cerrato, S. Morandi, V. Capucci, Pigmentary TiO_2: A challenge for its use as photocatalyst in NO_X air purification, Chem. Eng. J., 261 (2015) 76-82.

[16] M. Mishra, D.-M. Chun, α-Fe_2O_3 as a photocatalytic material: A review, Appl. Catal. A: Gen., 498 (2015) 126-141.

[17] D.A. Wheeler, G. Wang, Y. Ling, Y. Li, J.Z. Zhang, Nanostructured hematite: synthesis, characterization, charge carrier dynamics, and photoelectrochemical properties, Energy Environ. Sci., 5 (2012) 6682-6702.

[18] H. Xie, Y. Li, S. Jin, J. Han, X. Zhao, Facile Fabrication of 3D-Ordered Macroporous Nanocrystalline Iron Oxide Films with Highly Efficient Visible Light Induced Photocatalytic Activity, J. Phys. Chem. C, 114 (2010) 9706-9712.

[19] Y. Shi, H. Li, L. Wang, W. Shen, H. Chen, Novel α-Fe_2O_3/CdS Cornlike Nanorods with Enhanced Photocatalytic Performance, ACS Appl. Mater. Interfaces, 4 (2012) 4800-4806.

[20] W. Sun, Q. Meng, L. Jing, D. Liu, Y. Cao, Facile Synthesis of Surface-Modified Nanosized α-Fe_2O_3 as Efficient Visible Photocatalysts and Mechanism Insight, J. Phys. Chem. C, 117 (2013) 1358-1365.

[21] D. Barreca, G. Carraro, A. Gasparotto, C. Maccato, F. Rossi, G. Salviati, M. Tallarida, C. Das, F. Fresno, D. Korte, U.L. Štangar, M. Franko, D. Schmeisser, Surface Functionalization of Nanostructured Fe_2O_3 Polymorphs: From Design to Light-Activated Applications, ACS Appl. Mater. Interfaces, 5 (2013) 7130-7138.

[22] X. Zhou, Q. Xu, W. Lei, T. Zhang, X. Qi, G. Liu, K. Deng, J. Yu, Origin of Tunable Photocatalytic Selectivity of Well-Defined α-Fe_2O_3 Nanocrystals, Small, 10 (2014) 674-679.

[23] J. Balbuena, M. Cruz-Yusta, A.L. Cuevas, M.C. Lopez-Escalante, F. Martin, A. Pastor, L. Sanchez, Enhanced activity of a-Fe_2O_3 for photocatalytic NO removal, RSC Adv., 6 (2016) 92917-92922.

[24] R. Sugrañez, J. Balbuena, M. Cruz-Yusta, F. Martín, J. Morales, L. Sánchez, Efficient behaviour of hematite towards the photocatalytic degradation of NO_X gases, Appl. Catal. B: Environ., 165 (2015) 529-536.

[25] Y. Wang, H. Huang, J. Gao, G. Lu, Y. Zhao, Y. Xu, L. Jiang, TiO_2-SiO_2 composite fibers with tunable interconnected porous hierarchy fabricated by single-spinneret electrospinning toward enhanced photocatalytic activity, J. Mater. Chem. A, 2 (2014) 12442-12448.

[26] B. Tan, X. Zhang, Y. Li, H. Chen, X. Ye, Y. Wang, J. Ye, Anatase TiO_2 Mesocrystals: Green Synthesis, In Situ Conversion to Porous Single Crystals, and Self-Doping Ti^{3+} for Enhanced Visible Light Driven Photocatalytic Removal of NO, Chem. Eur. J., 23 (2017) 5478-5487.

[27] J. Sundaramurthy, P.S. Kumar, M. Kalaivani, V. Thavasi, S.G. Mhaisalkar, S. Ramakrishna, Superior photocatalytic behaviour of novel 1D nanobraid and nanoporous α-Fe_2O_3 structures, RSC Adv., 2 (2012) 8201-8208.

[28] S. Zhan, D. Chen, X. Jiao, S. Liu, Facile fabrication of long α-Fe_2O_3, α-Fe and γ-Fe_2O_3 hollow fibers using sol–gel combined co-electrospinning technology, J. Colloid Interface Sci., 308 (2007) 265-270.

[29] E. Cynthia, B. Arnaud, S. Vincent, P. Jean-Claude, A. Roy, M. Yves, K. Randa, K. Antonio, M. Philippe, Iron-based 1D nanostructures by electrospinning process, Nanotechnology, 21 (2010) 125701.

[30] F. Mou, J.-g. Guan, W. Shi, Z. Sun, S. Wang, Oriented Contraction: A Facile Nonequilibrium Heat-Treatment Approach for Fabrication of Maghemite Fiber-in-Tube and Tube-in-Tube Nanostructures, Langmuir, 26 (2010) 15580-15585.

[31] V.P. Torchilin, T.S. Levchenko, K.R. Whiteman, A.A. Yaroslavov, A.M. Tsatsakis, A.K. Rizos, E.V. Michailova, M.I. Shtilman, Amphiphilic poly-N-vinylpyrrolidones:: synthesis, properties and liposome surface modification, Biomaterials, 22 (2001) 3035-3044.

[32] G. Wang, H. Wang, J. Bai, Z. Ren, J. Bai, PVP-assisted assembly of lanthanum carbonate hydroxide with hierarchical architectures and their luminescence properties, Chem. Eng. J., 214 (2013) 386-393.

[33] N. Gacem, P. Diao, Effect of solvent polarity on the assembly behavior of PVP coated rhodium nanoparticles, Colloids Surf. A, 417 (2013) 32-38.

[34] K. Nayani, H. Katepalli, C.S. Sharma, A. Sharma, S. Patil, R. Venkataraghavan, Electrospinning Combined with Nonsolvent-Induced Phase Separation To Fabricate Highly Porous and Hollow Submicrometer Polymer Fibers, Ind. Eng. Chem. Res., 51 (2012) 1761-1766.

[35] H. Tanaka, T. Araki, Surface effects on spinodal decomposition of incompressible binary fluid mixtures, EPL (Europhysics Letters), 51 (2000) 154.

[36] E.P. Favvas, A.C. Mitropoulos, What is spinodal decomposition, J. Eng. Sci. Technol. Rev., 1 (2008) 25-27.

[37] W. Zhang, E. Mele, Phase separation events induce the coexistence of distinct nanofeatures in electrospun fibres of poly (ethyl cyanoacrylate) and polycaprolactone, Mater. Today Commun., 16 (2018) 135-141.

[38] C.M. Elliot, The Cahn-Hilliard Model for the Kinects of Phase Separation, in: J.F. Rodrigues (Ed.) Mathematical Models for Phase Change Problems - International Series of Numerical Mathematics, Birkhäuser Verlag Basel, 1989.

[39] V. Thavasi, G. Singh, S. Ramakrishna, Electrospun nanofibers in energy and environmental applications, Energy Environ. Sci., 1 (2008) 205-221.

[40] D. Bersani, P.P. Lottici, A. Montenero, Micro-Raman investigation of iron oxide films and powders produced by sol–gel syntheses, J. Raman Spectrosc., 30 (1999) 355-360.

[41] A.A. Tahir, K.G.U. Wijayantha, S. Saremi-Yarahmadi, M. Mazhar, V. McKee, Nanostructured α-Fe_2O_3 Thin Films for Photoelectrochemical Hydrogen Generation, Chem. Mater., 21 (2009) 3763-3772.

[42] J. Morales, L. Sánchez, F. Martín, F. Berry, X. Ren, Synthesis and Characterization of Nanometric Iron and Iron-Titanium Oxides by Mechanical Milling:: Electrochemical Properties as Anodic Materials in Lithium Cells, J. Electrochem. Soc., 152 (2005) A1748-A1754.

[43] R.S. Schrebler, L. Ballesteros, A. Burgos, E.C. Muñoz, P. Grez, D. Leinen, F. Martín, J. Ramón Ramos-Barrado, E.A. Dalchiele, Electrodeposited Nanostructured α-Fe_2O_3 Photoanodes for Solar Water Splitting: Effect of Surface Co-Modification on Photoelectrochemical Performance, J. Electrochem. Soc., 158 (2011) D500-D505.

[44] K. Sing, The use of nitrogen adsorption for the characterisation of porous materials, Colloids Surf. A, 187–188 (2001) 3-9.

[45] R.J. Lewis, N.I. Sax, Sax's Dangerous Properties of Industrial Materials, 12th ed., Van Nostrand Reinhold, New York, 2012.

[46] K.I. Hadjiivanov, Identification of Neutral and Charged Surface NO_X Species by IR Spectroscopy, Catal. Rev. Sci. Eng., 42 (2000) 71-144.

[47] J. Sá, J.A. Anderson, FTIR study of aqueous nitrate reduction over Pd/TiO_2, Appl. Catal. B: Environ., 77 (2008) 409-417.

[48] B. Zhao, R. Ran, X. Wu, D. Weng, X. Wu, C. Huang, Comparative study of Mn/TiO_2 and Mn/ZrO_2 catalysts for NO oxidation, Catal. Commun., 56 (2014) 36-40.

[49] J. Ma, H. He, F. Liu, Effect of Fe on the photocatalytic removal of NO_X over visible light responsive Fe/TiO_2 catalysts, Appl. Catal. B: Environ., 179 (2015) 21-28.

[50] J. Ma, H. Wu, Y. Liu, H. He, Photocatalytic Removal of NO_X over Visible Light Responsive Oxygen-Deficient TiO_2, J. Phys. Chem. C, 118 (2014) 7434-7441.

[51] J. Ma, C. Wang, H. He, Enhanced photocatalytic oxidation of NO over g-C_3N_4-TiO_2 under UV and visible light, Appl. Catal. B: Environ., 184 (2016) 28-34.

[52] N. Todorova, T. Giannakopoulou, S. Karapati, D. Petridis, T. Vaimakis, C. Trapalis, Composite TiO_2/clays materials for photocatalytic NO_X oxidation, Appl. Surf. Sci., 319 (2014) 113-120.

[53] Y. Duan, J. Luo, S. Zhou, X. Mao, M.W. Shah, F. Wang, Z. Chen, C. Wang, TiO_2-supported Ag nanoclusters with enhanced visible light activity for the photocatalytic removal of NO, Appl. Catal. B: Environ., 234 (2018) 206-212.

[54] J. Yao, Y. Zhang, Y. Wang, M. Chen, Y. Huang, J. Cao, W. Ho, S.C. Lee, Enhanced photocatalytic removal of NO over titania/hydroxyapatite (TiO2/HAp) composites with improved adsorption and charge mobility ability, RSC Adv., 7 (2017) 24683-24689.

[55] J.Z. Bloh, A. Folli, D.E. Macphee, Photocatalytic NO_X abatement: why the selectivity matters, RSC Adv., 4 (2014) 45726-45734.

Table 1. Crystal size, surface area and porosity parameters for α-Fe_2O_3 samples.

Samples	**H_nanotubes**	**H_flakes**	**TiO_2 P25**
Crystal size (nm)	54	66	30
Surface Area			
A_{BET} / $m^2 \cdot g^{-1}$ [a]	13.61	13.79	57.25
$A_{micropore}$ / $m^2 \cdot g^{-1}$ [b]	11.91	6.63	8.05
$A_{External}$ / $m^2 \cdot g^{-1}$ [b]	1.70	7.17	49.20

[a] Determined by adsorption of N_2 at 77 K, BET method
[b] Determined from the N_2 adsorption isotherm by t-plot method

Figure captions

Fig. 1: SEM images of the H_nanotubes sample: (a)(b) Fe_2O_3 mat of interconnected nanotubes, (c) open microtube and (d) detail of the microtube wall.

Fig. 2: SEM images of the H_flakes sample: (a) image of a wrapped film; (b) detail of the wall wrapped lamella cross section; (c) image of the surface flat lamella and (d) cross section.

Scheme 1: Illustration of the growth process for the H_nanotubes and H_flakes samples.

Fig. 3: (a) XRD patterns and (b) Raman spectra obtained for hematite porous samples. (c) XPS spectra of the Fe2p and Fe3p (inset) regions corresponding to the H_nanotubes sample.

Fig. 4: (a) N_2 adsorption-desorption Isotherms for H_nanotubes and H_flakes samples. (b) Kubelka-Munk transformed reflectance spectra for the H_nanotubes sample.

Fig. 5: (a) NO gas concentration profile evolution measured during the photochemical test, for hematite porous samples and TiO_2-P25. (b) NO and NO_X conversion, NO_2 released and selectivity values. (c) NO_2 absorption ability of samples in the darkness.

Graphical Abstract (for review)

Hematite porous architectures as enhanced air purification photocatalyst

José Balbuena, Manuel Cruz-Yusta, Ana L. Cuevas, Francisco Martín, A. Pastor, R. Romero and Luis Sánchez **

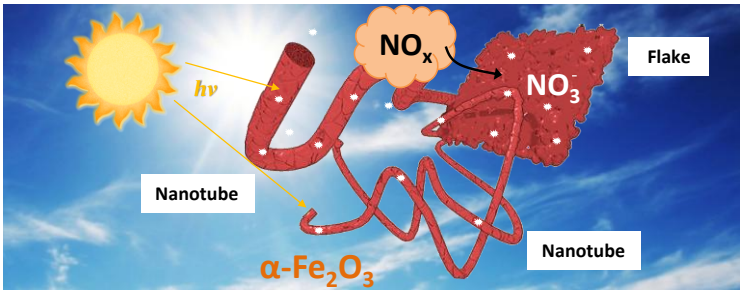

Highlights

- Porous architectures act as new enhanced Fe_2O_3 photocatalysts in De-NO_X processes
- A high NO conversion efficiency similar to that of TiO_2 P25 is obtained
- The adsorption of NO_2 molecules is facilitated by the large micropore area

Figure

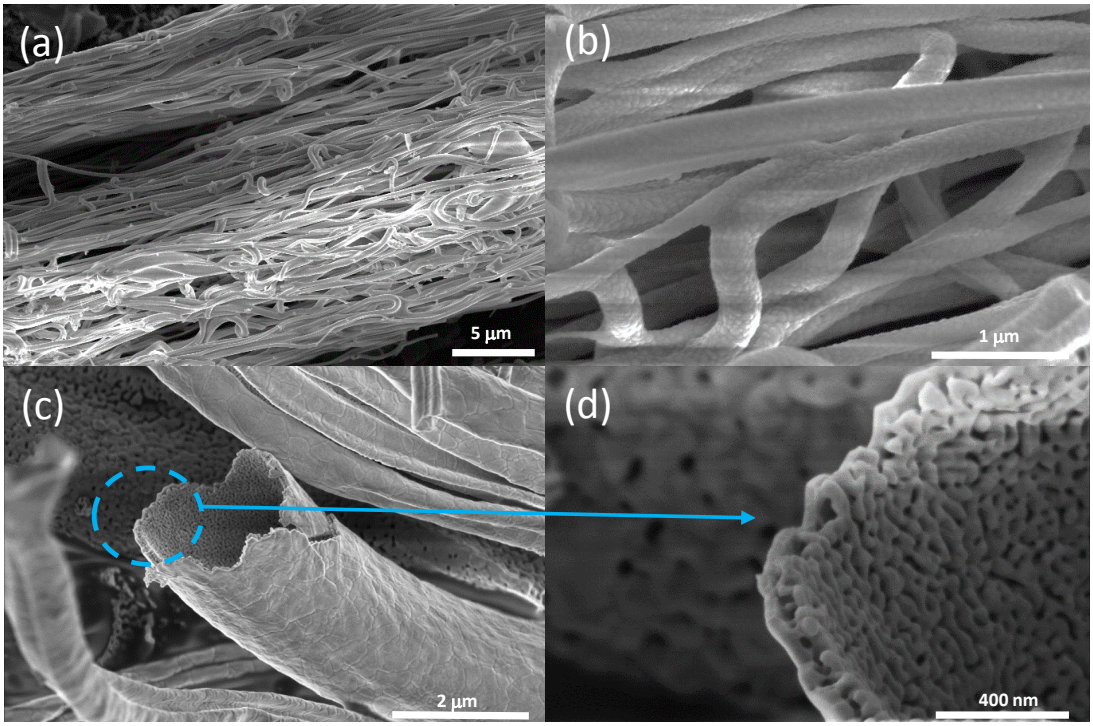

Figure 1

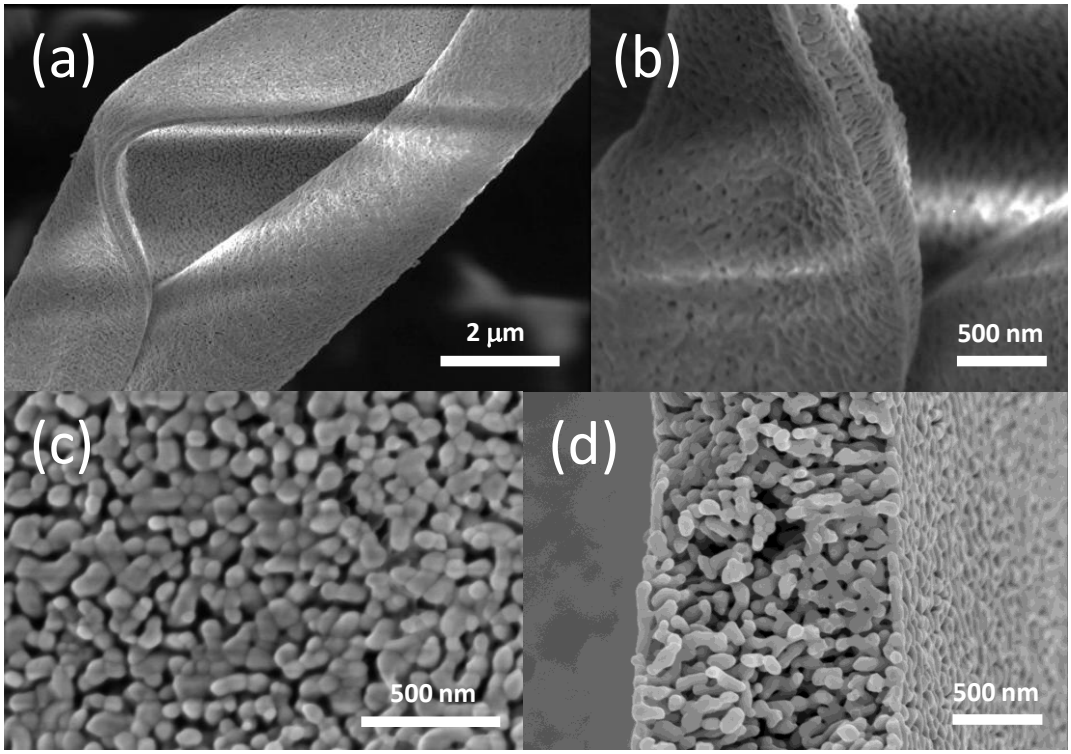

Figure 2

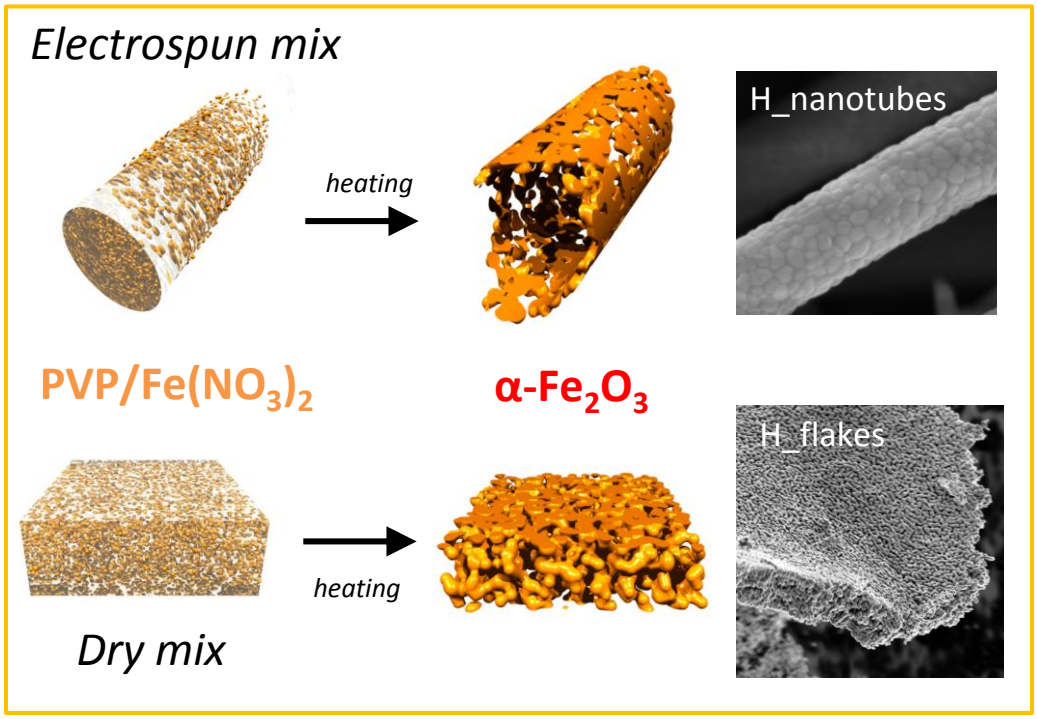
Electrospun mix
heating
H_nanotubes
PVP/Fe(NO3)2
α-Fe2O3
H_flakes
heating
Dry mix

Scheme 1

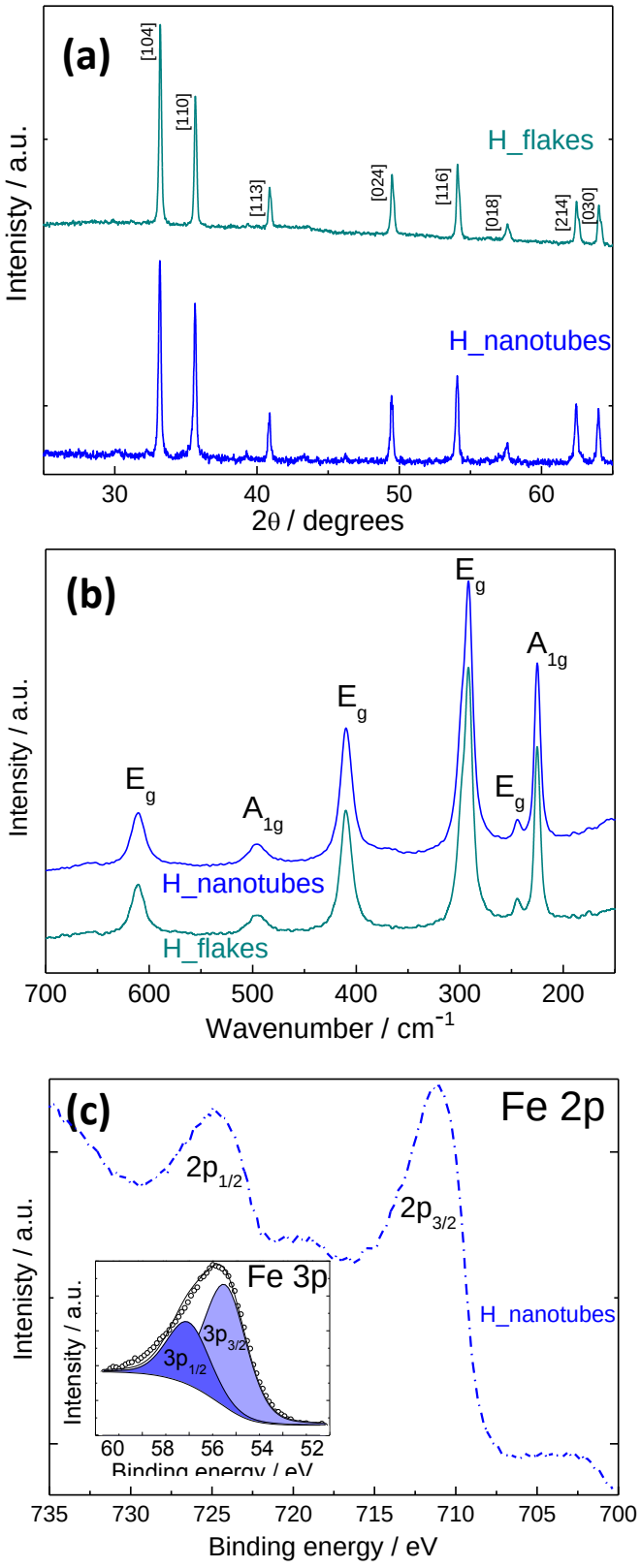
(a)
[104]
[110]
[113]
[024]
[116]
[018]
[214]
[030]
H_flakes
H_nanotubes
Intenisty / a.u.
30
40
50
60
2θ / degrees
(b)
E_g
A_1g
E_g
E_g
A_1g
E_g
H_nanotubes
H_flakes
Intensity / a.u.
700
600
500
400
300
200
Wavenumber / cm^-1
(c)
Fe 2p
2p_1/2
2p_3/2
H_nanotubes
Fe 3p
3p_3/2
3p_1/2
Intensity / a.u.
60
58
56
54
52
Binding energy / eV
Intenisty / a.u.
735
730
725
720
715
710
705
700
Binding energy / eV

Figure 3

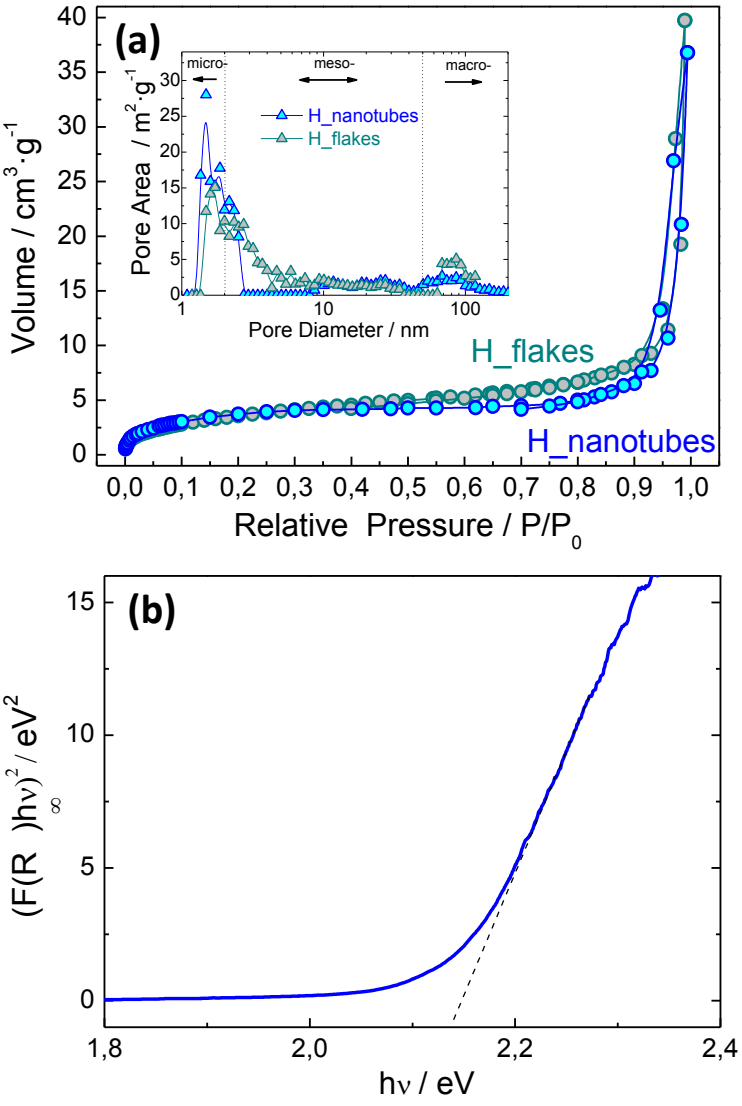
(a)
Volume / cm3·g-1
Relative Pressure / P/P0
H_flakes
H_nanotubes
micro-
meso-
macro-
Pore Area / m2·g-1
Pore Diameter / nm
H_nanotubes
H_flakes
(b)
(F(R∞)hν)2 / eV2
hν / eV

Figure 4

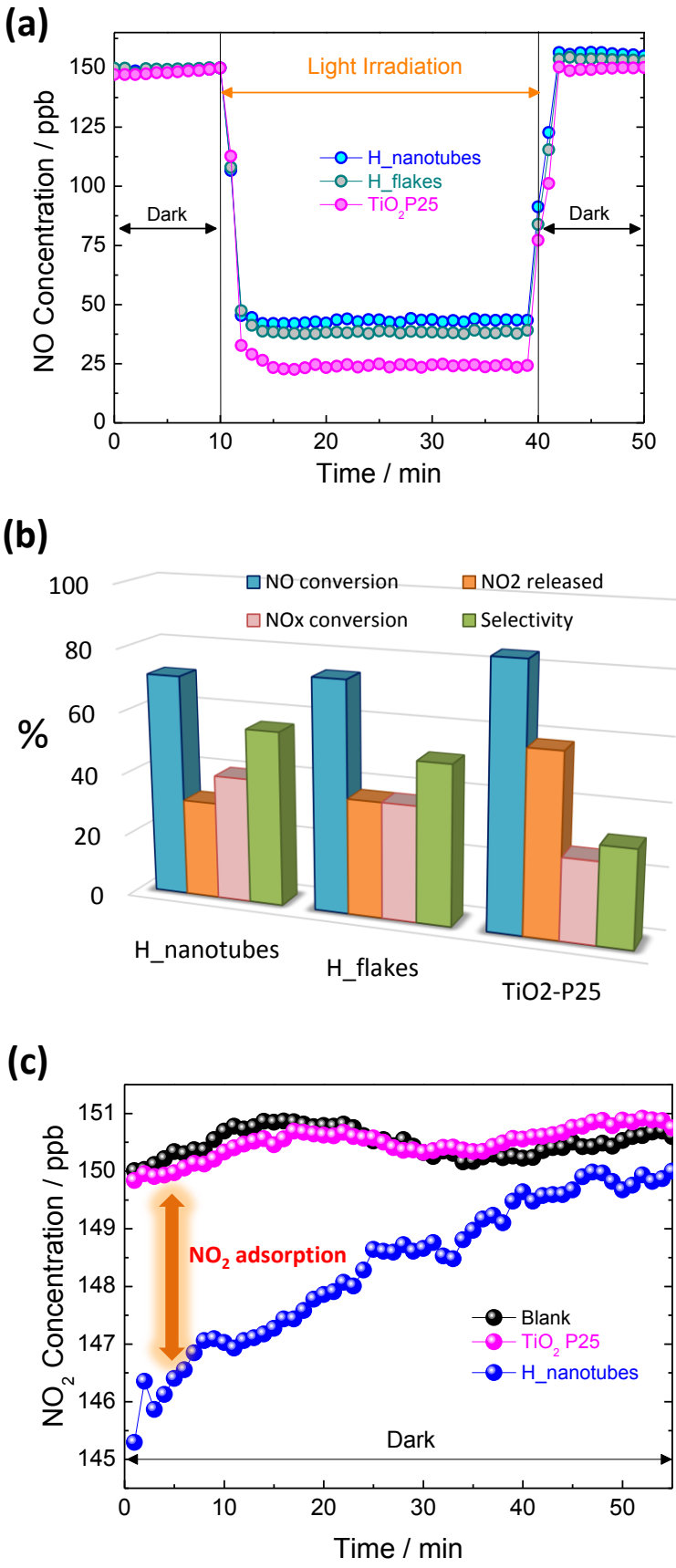
(a)
Light Irradiation
H_nanotubes
H_flakes
TiO2P25
Dark
Dark
NO Concentration / ppb
Time / min
(b)
NO conversion
NO2 released
NOx conversion
Selectivity
%
H_nanotubes
H_flakes
TiO2-P25
(c)
NO2 adsorption
Blank
TiO2 P25
H_nanotubes
Dark
NO2 Concentration / ppb
Time / min

Figure 5